

The λ -Orionis Ring in CO

W.J. Lang¹, M.R.W. Mashed¹, T.M. Dame², and P. Thaddeus²

¹ H.H. Wills Physics Laboratory, Bristol University, Bristol, BS8 1TL, UK

² Harvard-Smithsonian Center for Astrophysics, 60 Garden St., Cambridge, MA 02138, USA

Received 2 June 1999 / Accepted 18 February 2000

Abstract. The results of a new CO(J=1→0) survey of the ring of molecular clouds around the H II region Sh-2-264 and the λ -Orionis OB-association are presented. The distribution of molecular gas closely approximates that of the dust seen in IRAS emission. The total molecular mass is $1.4 \times 10^4 M_{\odot}$. The mass spectrum of the emission clumps is a power-law with index -1.8, similar to that observed in other star-forming regions. The kinematics of the ring are modelled, but its alignment close to the plane of the sky allows only very weak constraints on expansion velocity and the age of the system. The data are compared with previous surveys, and possible evolutionary schemes for the region discussed.

Key words: ISM: clouds – Galaxy: structure – radio lines: ISM – ISM: molecules – ISM: bubbles

1. Introduction

In addition to the familiar subgroups a-d of the Orion OB1 association, the Orion star forming complex contains the O8 III_f star λ -Ori, and its accompanying cluster of 12 B stars. Using photometric techniques Murdin & Penston (1977) estimated the distance to the cluster to be 400 pc, the value adopted in this paper. The optical nebulosity around the cluster was first recorded by Barnard (1894) but it was some years before the region received further attention. Barnard included the dark clouds surrounding this emission in his 1927 catalogue, and the H II region itself was Sh-2-264 in the Sharpless catalogue (1959). Later authors (eg. Morgan et al. 1955) noted the wide angular extent ($\sim 8^{\circ}$) of the nebula. The Ring of dark clouds was further mapped by Khavtassi (1960) and Lynds (1962).

The Ring was considered a prime target for the early HI investigations, largely because of its apparent high degree of symmetry and distance from the obscuration of the Galactic plane. Wade (1957, 1958a,b) surveyed a slice through the central part of the nebula, and claimed to discover an expanding shell of atomic hydrogen. Further HI mapping by Zhang & Green (1991) showed that Wade's one-dimensional data could easily be misinterpreted, as the slice happened to pass through the

densest parts of the Ring and thus was not representative of the underlying structure. However, there was evidence for an HI 'hole', the existence of which was subsequently confirmed in the Dwingeloo HI Survey (Hartmann & Burton 1997).

The Ring was first mapped in CO by Maddalena et al. (1986) and Maddalena & Morris (1987; henceforth 'MM') as part of a large scale survey of the Orion region. Although these observations had significantly lower area coverage and sensitivity than the present survey, they demonstrated the existence of a molecular ring. The full extent and symmetry of the Ring are strikingly displayed in the far infra-red IRAS survey (Zhang et al. 1989 and references therein). The peaks in the 100 μ m emission correspond well with those in the MM survey but the IRAS observations also showed the extensive ring structure in low level emission not seen in the MM data. (See Fig. 10, below)

It is plausible to treat the Ring and the OB stars as an interacting system of common origin. The stars lie close to the centre of the Ring and the IRAS maps show that they are embedded in a warm dust cloud, which despite the strong UV-field still has a molecular component in the weak filamentary emission seen in the present survey with a peak at a radial velocity of $\approx 4 \text{ km s}^{-1}$. Measurements by Wilson (1963) give the radial velocity of the star λ Ori as $v_{\text{LSR}} = 18 \pm 0.5 \text{ km s}^{-1}$. This lies outside the velocity range of the ring and of the H II region according to all other measurements and may be a further example of the typical radial velocity difference between exciting stars and clouds in young clusters of the order of 10 km s^{-1} noticed by Leisawitz et al. (1989). The reasons for this difference are not clear. Various ideas have attempted to explain this anomaly, for example the theory that the Ring is the result of a supernova (eg. Cunha & Smith 1996) with λ -Ori as the erstwhile binary companion to its progenitor. However, for the purposes of this paper the common origin of the OB stars and the Ring is assumed.

2. Observations

The data were gathered during the period October 1995 to December 1996 with the CfA 1.2 m Telescope, which has HPBW 8.4 at 115 GHz . The technical specifications of the telescope are given elsewhere (eg. Cohen et al. 1986), and the SIS receiver is described by Pan et al. (1983). The configuration of the telescope and observing parameters of the survey are listed

Table 1. Survey and telescope parameters

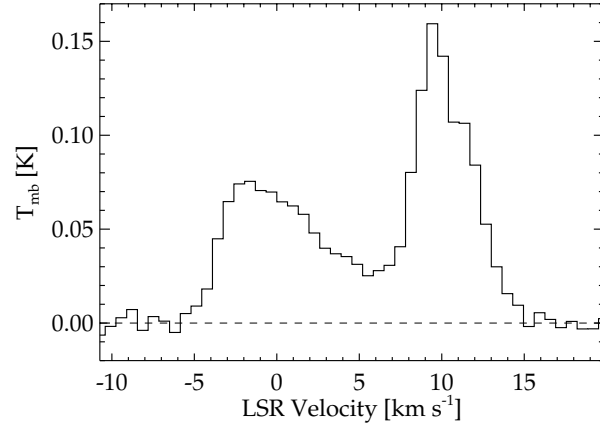
Parameter	Value
Observing mode	Frequency switching
Switching interval	10 MHz
Spatial coverage	$191^\circ \leq l \leq 201^\circ$ $-18^\circ \leq b \leq -7^\circ$
HPBW Main Beam	8'.4
Beam efficiency	0.82
Receiver Temperature	70 ± 5 K (SSB)
Water opacity (τ_w)	0.05–0.25
Integration times	5–30 seconds
Velocity resolution	0.65 km s^{-1}
Sensitivity per channel	$T_{mb}=0.25$ K
Sampling interval	3'.75
Total number of spectra	28 885

in Table 1. Observations were made on a uniform rectangular grid aligned to Galactic coordinates (l, b). The grid spacing was 3'.75 to achieve a fully sampled survey.

Calibration was performed by means of a black-body chopper-wheel (Kutner 1977) before each observation. Frequent observations of standard sources showed that variations in intensity calibration were almost always less than 5%. A velocity resolution of 0.65 km s^{-1} was provided by a 256-channel filter bank covering a bandwidth of 64 MHz. The spectra were obtained in frequency-switching mode, with a switching interval of 10 MHz. Third- or fourth- order polynomial baselines were fitted to emission-free parts of the spectra and subtracted. After folding the rms noise per channel was 0.25 K.

When CO observations are obtained by frequency switching, they may be contaminated by line emission from atmospheric CO in a layer at an altitude between 50 and 100 km, depending on latitude and season. The atmospheric line was modelled by summing all spectra for which it was not blended with the celestial CO emission obtained during a single observing shift, scaling them by airmass. A Voigt profile was then fitted at the known position of the line in the spectrum. This profile was based on the assumption, adequate for this purpose, that the CO is in a thin layer in the atmosphere. This estimate of the atmospheric contribution was then removed from each of the individual spectra, again scaling for elevation. Since in most spectra the celestial CO emission is not blended with the atmospheric line, this method results in only very small errors in the astronomical signal. Its largest contribution to any of the maps shown here is 0.03 K km s^{-1} or 0.01 K deg .

The spectra were combined into a datacube, which was then gaussian-smoothed to $10'$ resolution with 0.12 K sensitivity. To obtain the best signal to noise ratio in the two-dimensional maps, the integrations along the axes of the datacube used the masked moment technique used in previous surveys (eg. Oliver et al. 1996, Digel et al. 1996). This procedure reduces the noise by removing the contribution of emission-free channels to the integrations by accepting only volumes in the datacube where the signal smoothed over the mask exceeds a cutoff value. Here a mask of 3 pixels in each of the 3 directions was used with a

**Fig. 1.** CO emission averaged over the whole survey area.

cutoff level of 0.1 K, approximately the mean rms noise of the gaussian-smoothed datacube. We refer to maps produced in this way as ‘moment’ maps. This method has the added advantage here of excluding almost all remaining atmospheric emission.

3. Results

Fig. 1 is the total emission profile of CO, averaged over the entire survey region shown in Fig. 2. It is evident that the emission is strongly double-peaked; the two main velocity features are a wide peak with an approximate FWHM of $6\text{--}7 \text{ km s}^{-1}$ at -2 km s^{-1} , and a brighter, narrower peak with $\text{FWHM} \approx 5 \text{ km s}^{-1}$ at velocity 9 km s^{-1} . As we show below, the asymmetry of both features results from an ensemble of clouds with a range of velocities.

3.1. The maps

Fig. 2 shows the velocity-integrated CO emission, W_{CO} obtained by the masked moment technique and Fig. 3 shows the corresponding (v, l) and (v, b) moment maps integrated over b and l respectively.

More detailed information of the emission is shown in the channel maps of Fig. 4. Each panel shows a map of W_{CO} in a velocity interval 1.95 km s^{-1} wide centered on the velocity shown. This value for the width was chosen to match three channels of the original spectra. Again the double-peaked (Galactic) north/south structure is dominant, though there is little in the way of intermediate-velocity material around the central latitudes that we may expect from a continuous ring.

The emission with $W_{\text{CO}} > 0.325 \text{ K km s}^{-1}$ covers an area of $\sim 36 \text{ deg}^2$, approximately one third of that surveyed. These maps are considerably more sensitive than the MM survey whose lowest contour lies at approximately 3.5 K km s^{-1} , 10 times higher than the lowest contour of the present survey. As may be seen in Fig. 10, much of the ring observed by IRAS corresponds to CO that lies below the sensitivity of MM. Fig. 5 shows a histogram of W_{CO} values of the present survey compared the approximate sensitivity limit of the MM survey. 78% of the total area of emission in the new survey was undetected by MM, but this weak

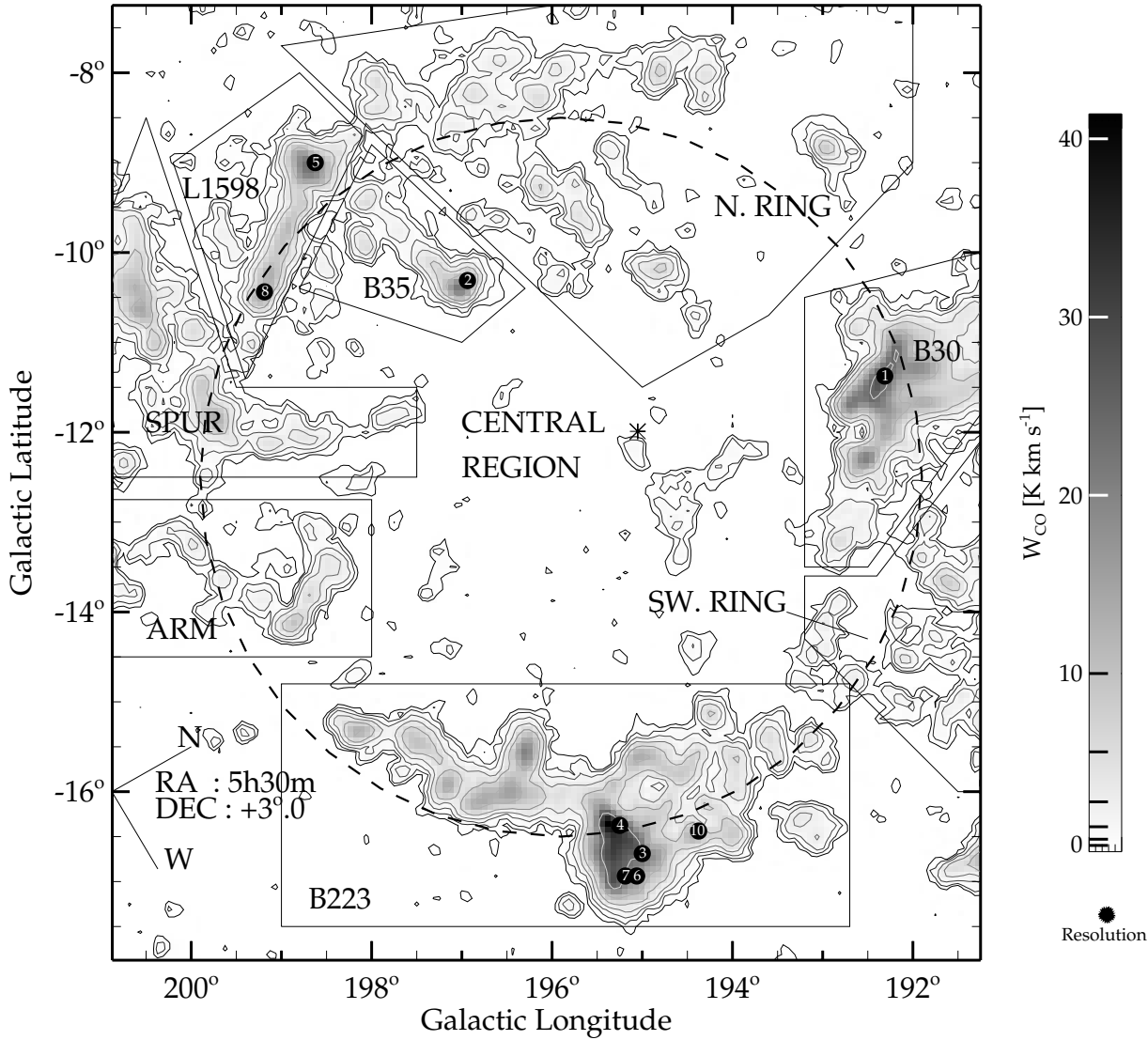


Fig. 2. Moment map of velocity-integrated emission, W_{CO} . Contours are logarithmic at 0.325, 0.65, 1.3, 2.6, ... K km s⁻¹. The map covers the velocity range $[-10, +20]$ km s⁻¹ with respect to the LSR. Boxes mark the subregions discussed in Sect. 4, and the dashed line shows the (l, b) projection of the best fit ring model derived in Sect. 7. The positions of the 10 brightest clump peaks are marked, with their numbers from Table 2. The spatial smoothing to $10'$ slightly reduces the survey area, so Clump 9 lies slightly off the bottom right corner of the map. The position of λ -Ori is shown by * near $(195^\circ, -12^\circ)$

emission contributes only 28% of the total W_{CO} . No significant emission was found outside the velocity range of Fig. 3, unsurprising given the Ring's large displacement from the Galactic plane.

3.2. Mass estimates

We define M_{CO} as the molecular cloud mass derived on the assumption that the velocity-integrated CO intensity, W_{CO} , is directly proportional to the H_2 column density, $N_{\text{H}_2}/W_{\text{CO}}$. Here we use the conversion factor, $X = N_{\text{H}_2}/W_{\text{CO}} = 1.1 \times 10^{20} \text{ cm}^{-2} (\text{K km s}^{-1})^{-1}$ as derived by Digel et al. (1995) by comparing EGRET gamma-ray emission with CO data from the Maddalena et al. Orion survey.

Following previous conventions (e.g. Dame et al. 1986; Appendix A of Williams et al. 1994), we define the virial mass such that virial equilibrium between kinetic energy and potential energy would be satisfied, with $M_{\text{vir}} = kR\Delta v^2$, where R is the effective radius of the cloud, and Δv the FWHM of the CO emission. Here k is a constant of proportionality which depends weakly on the assumed radial density profile of clouds. For uniform density, $k = 210 M_\odot \text{ pc}^{-1} \text{ km}^{-2} \text{ s}^2$ (eg. Bertoldi & McKee 1992).

The assumption of virial equilibrium for a cloud means that M_{vir} is an upper limit mass estimate for unbound clouds. For such clouds the luminosity mass, M_{CO} may provide a more reliable and consistent measure of cloud mass. The linewidth which determines the virial mass is affected by additional forces

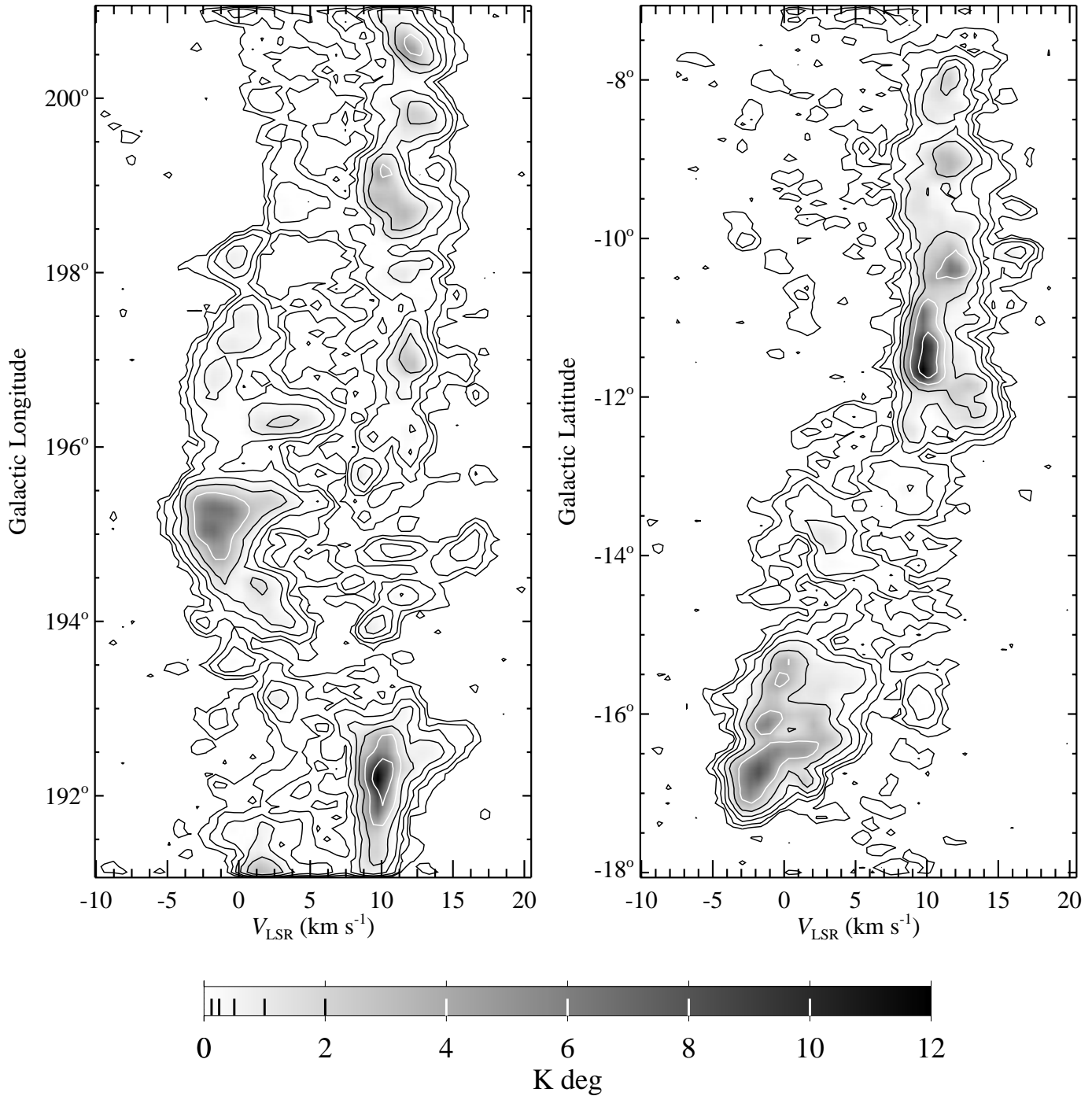


Fig. 3. (v, l) and (v, b) maps, integrated over the entire latitude and longitude range respectively. Contours are at 0.12, 0.24, 0.48, 0.96, 1.92..... K deg.

due to magnetic fields, and generally M_{vir} becomes a poor tracer of true mass in smaller clouds (Maloney 1990). Summing W_{CO} over the total area of emission gives a total mass of the Ring of $1.37 \times 10^4 M_{\odot}$.

The CO emission from the Ring has a highly fragmented, or clumpy, appearance (Fig. 2). To compare this fragmentation with observations of other molecular clouds (e.g. Blitz 1991) the datacube was analysed using the *Clumpfind* algorithm of

Williams et al. (1994), of which the brief description given here is taken directly from their paper. The method starts at the highest contour level and works down through lower levels. At each level, isolated contours are identified and labeled as new clumps. The other contours at the level are extensions of previously defined clumps. Contours that surround just one peak are simply assigned to the corresponding clump, but blended contours that surround more than one peak are split up by a “friends of

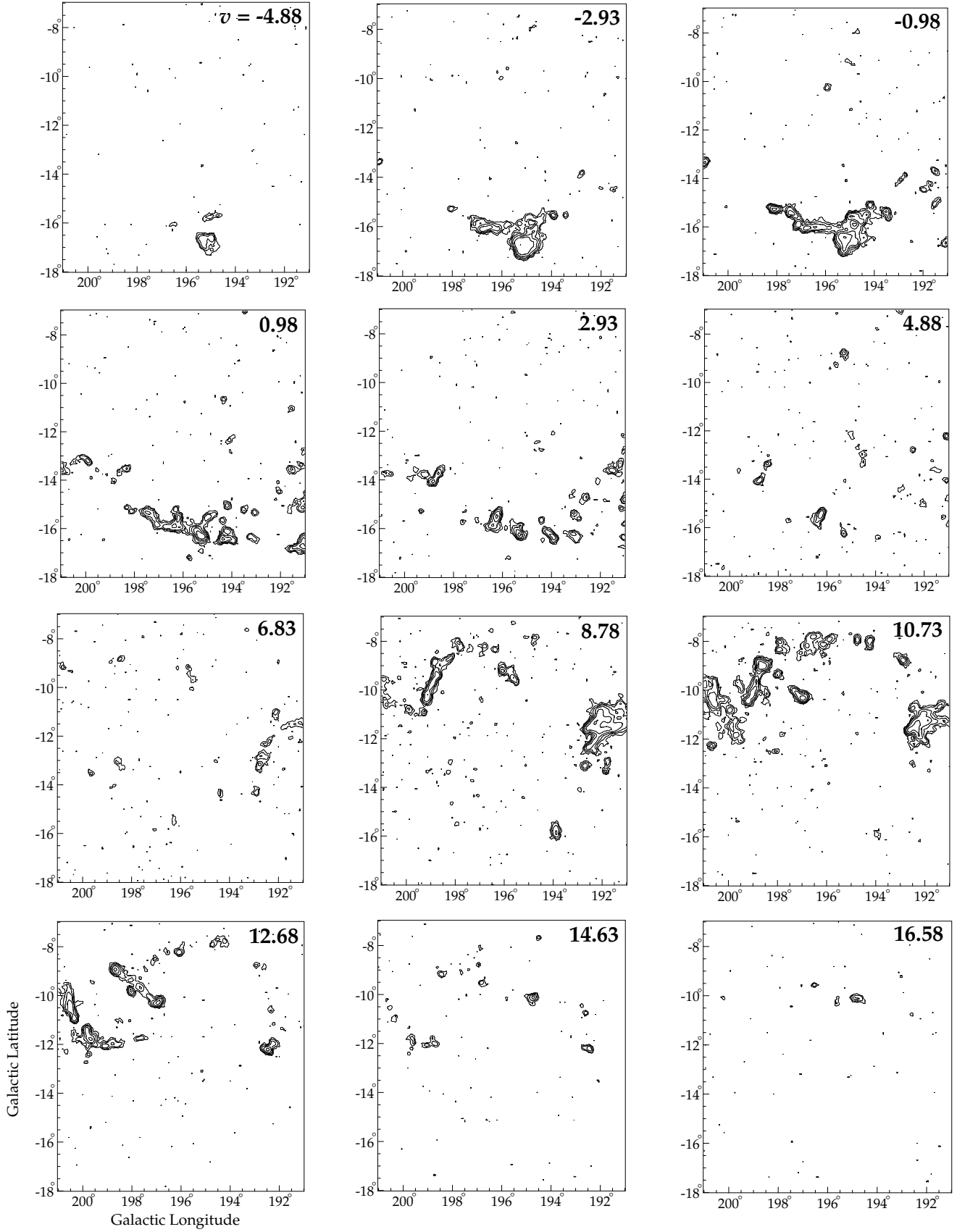


Fig. 4. Channel maps of W_{CO} integrated over three channels of the original spectra. The velocity width for each map is 1.95 km s^{-1} centred on the velocities shown in the panels. The contour levels start at 0.5 K km s^{-1} and increase by factors of 2.

Table 2. Clump parameters for the 10 brightest emission peaks detected by the *Clumpfind* algorithm, and the subregions of the Ring in which they are found. The columns give position within the dataset (l, b, v), maximum brightness temperature within the peak T_{max} , the approximate FWHM clump dimensions Δ_l, Δ_b and average FWHM linewidth Δ_v , the effective clump radius ($\sqrt{area/\pi}$), and the mass estimates M_{CO} and M_{vir} described in Sect. 3. The final column shows in which section of the Ring the clump is to be found. (See Fig. 2)

Ncl	l ($^\circ$)	b ($^\circ$)	v (km s^{-1})	T_{max} (K)	Δ_l (pc)	Δ_b (pc)	R (pc)	Δ_v (km s^{-1})	M_{CO} (M_\odot)	M_{vir} (M_\odot)	COMPLEX
1	192.31	-11.38	9.43	13.42	5.13	4.31	4.60	1.73	1967	868	B30
2	196.94	-10.31	12.03	10.75	1.18	1.08	1.44	1.66	219	250	B35
3	195.00	-16.69	-2.28	9.36	2.90	2.08	2.55	2.25	727	811	B223
4	195.25	-16.38	-0.33	9.35	2.66	2.20	2.62	4.14	854	2823	B223
5	198.63	-9.00	11.38	8.89	1.91	1.56	2.07	2.53	395	831	L1598
6	195.06	-16.94	-2.93	8.67	1.70	1.41	1.56	1.80	247	317	B223
7	195.19	-16.94	-2.93	8.51	1.09	2.11	1.71	2.45	422	640	B223
8	199.19	-10.44	10.08	7.99	1.26	2.04	1.75	1.58	216	276	L1598
9	191.06	-16.75	0.98	7.24	2.44	2.43	2.17	1.50	215	307	–
10	194.38	-16.44	0.98	6.22	1.70	1.38	1.88	2.58	127	786	B223

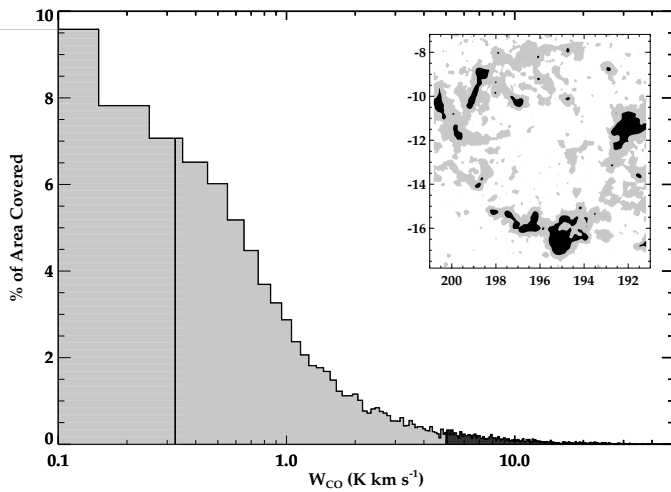


Fig. 5. A histogram of the integrated-emission in the new survey. The black area marks the extent of emission detected in the MM survey, while the grey area shows the substantial additional sensitivity of the new survey, revealing a wealth of low-level emission. The vertical line corresponds to the lowest contour shown in Fig. 2. Signals lower than this are considered to be contaminated by noise.

friends” algorithm described in the paper. In this way, the dataset is divided into 130 distinct clumps, with masses summing to $1.1 \times 10^4 M_\odot$, 80% of the total M_{CO} . The clumps are labelled according to the relative brightness of the peak temperatures within them, so clump 1 contains the emission maximum, but not necessarily the maximum W_{CO} or largest mass. *Clumpfind* parameters calculated for the clumps with the 10 brightest emission peaks are listed in Table 2. The full list of 130 clumps is available from the authors on request.

The luminosity masses of the clumps were binned in logarithmic intervals of $\Delta \log M = \log 2$. A histogram of these data is shown in Fig. 6. In the range 30–2000 M_\odot , this distribution approximates a power-law with index, -1.8 ± 0.2 . This exponent is similar to those measured in other star-forming regions (Blitz 1991; Digel et al. 1996).

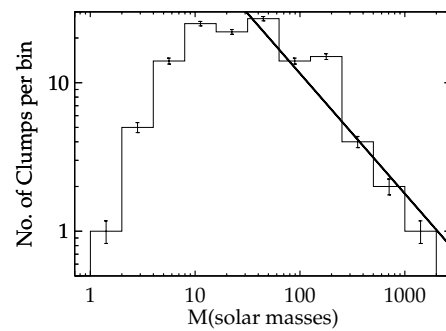


Fig. 6. Mass spectrum of clumps with power-law fit with slope, $dN/dM = -1.8$

4. Objects of interest

When the internal structure of the Ring is considered, several natural subgroups of clumps are apparent: the clouds associated with the Barnard objects B30, B223 and B35, the bar-shaped cloud containing the Lynds Dark Clouds L1598 and L1599, and several other distinct features which are marked in Fig. 2. The ‘Spur’ feature is named after a coincident radio continuum spur observed by Reich (1978). CO emission from several of these complexes is discussed briefly here.

4.1. B30

The brightest emission in the survey, both in terms of W_{CO} and T_{max} , comes from the cloud complex known as B30. This region also contains the Barnard clouds B31 and B32 and the Lynds clouds L1580–1584. Clump 1 here coincides with peak MM8 of the earlier CO survey. The bright-rimmed cloud at $\sim (193^\circ, -12^\circ)$ is L1582, previously mapped in detail by Zhou et al. (1988). It can be visually subdivided into two components. In the optically-bright globule closest to the λ Ori association lies the star HK Ori at $(192^\circ 64', -11^\circ 62')$, a type A4 peculiar variable, associated with the luminous IRAS point source 05284+1207. The association between these objects is typical of the close relationship between intermediate-mass stars and

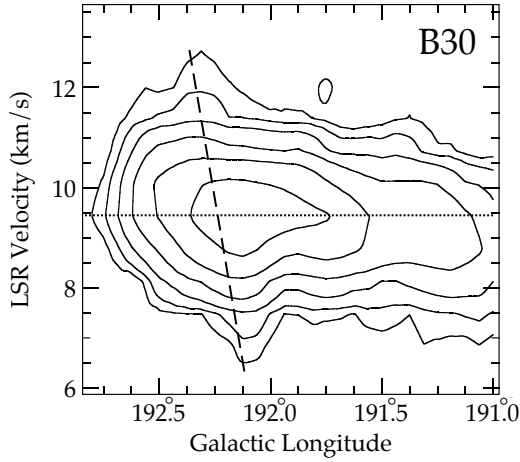


Fig. 7. The velocity structure of clump 1 in the B30 complex integrated over the latitude range $b = [-11^\circ, -10^\circ.5]$. The contours are at 0.15, 0.3, 0.6, 1.2, 2.4, 4.8 K. The dotted line marks the 9.4 km s^{-1} velocity of the clump peak and the dashed line shows the RNO 43 outflow. (Cabrit et al., 1988)

massive globules surrounding H II regions (e.g. Sugitani et al. 1989, 1991).

The other component of L1582 is the dark cloud at slightly greater radial distance from the OB stars. At the end of a dark finger of optical obscuration is a strong $2 \mu\text{m}$ source, embedded within the ammonia core L1582A (Benson et al. 1984). This extension of molecular gas into Sh-2-264 is associated with the end of the southern lobe of the Herbig-Haro object RNO 43. The young star driving the outflow is at $(192^\circ.158, -11^\circ.093)$, which has an infrared counterpart as IRAS 05293+1247. Higher resolution molecular-line studies (eg. Bence et al. 1996) suggest that the high brightness temperatures observed in this cloud arise partly from the large energy ($\sim 10^{50}$ erg) contributed by the outflow to the ambient cloud material. Outflow activity is associated with the earliest stages of star formation (possibly $t < 10^5$ yr), so it seems that there has been recent triggering along the edge of B30, which apparently possesses ionization fronts from interaction with the H II region. A position-velocity map (Fig. 7) for the B30 region shows the RNO43 outflow clearly, despite its orientation almost along the line of sight (Cabrit et al., 1988). Also noticeable is the velocity gradient across the B30 cloud, which may be attributed to a projection effect of the expanding shell.

4.2. The B35 Outflow

B35 is a bright-rimmed cometary globule, and is known to be the site of low-to-intermediate mass star formation. The nova variable FU Ori lies just behind the head of the globule, which is clump 2 of this survey. On the edge of this clump facing λ -Ori is the IRAS point source 05417+0907, also associated with an NH_3 core. Myers et al. (1988) discovered a powerful bipolar outflow here, the lobes of which are oriented almost along the line of sight. The (v, l) map in Fig. 8 has been obtained by integrating over a small latitude range ($\sim 1^\circ.5$). The CO outflow is

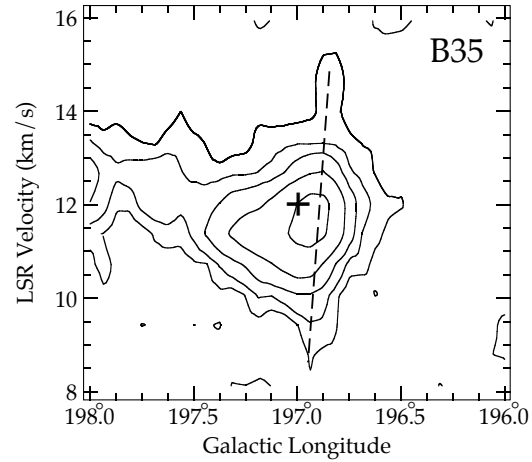


Fig. 8. A (v, l) CO map of B35 integrated over the latitude range $[-11^\circ, -9^\circ.5]$. The contours are at 0.15, 0.3, 0.6, 1.2, 2.4 K deg. The cross marks the position of the peak emission from clump 2 and the dashed line shows the path of the outflow associated with the clump.

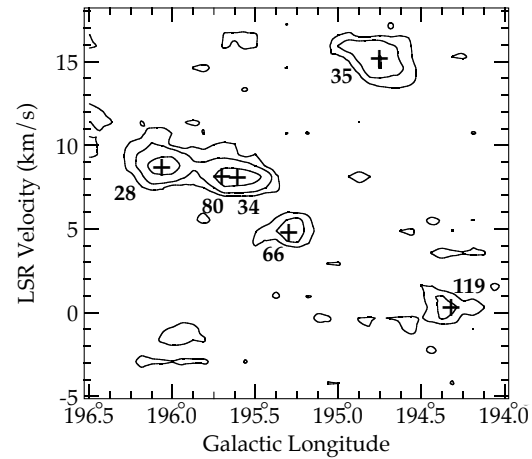


Fig. 9. The velocity structure of the diffuse filamentary emission around $(196^\circ, -10^\circ)$ in the northern section of the Ring, integrated over the range, $b = [-11^\circ, -8^\circ.5]$. The contours are at 0.19, 0.38 and 0.76 K deg. The peaks of each clump are marked with crosses and numbered.

clearly visible, spanning a velocity range of 6 km s^{-1} . Using an even smaller latitude range hints at further structure, and while admittedly very noisy, the resulting maps suggest an extended outflow consistent with the previous findings, with both lobes curving away from λ -Ori in response to stellar winds and ionizing radiation, over a total velocity range in excess of 10 km s^{-1} .

4.3. The Northern and Southwestern Ring regions

The Northern Ring differs from the brighter sections, in that it is not dominated by massive clumps at particular velocities. Instead, there are a large number of low mass clumps spread over some 20 km s^{-1} in velocity. The velocity structure of part of this region is shown in Fig. 9. Clumps 28, 34, 66, 80 and 119 appear to be related in the (l, b) map, forming a filament between $(197^\circ, -8^\circ)$ and $(194^\circ, -10^\circ.5)$. But Fig. 9 shows that clump 35

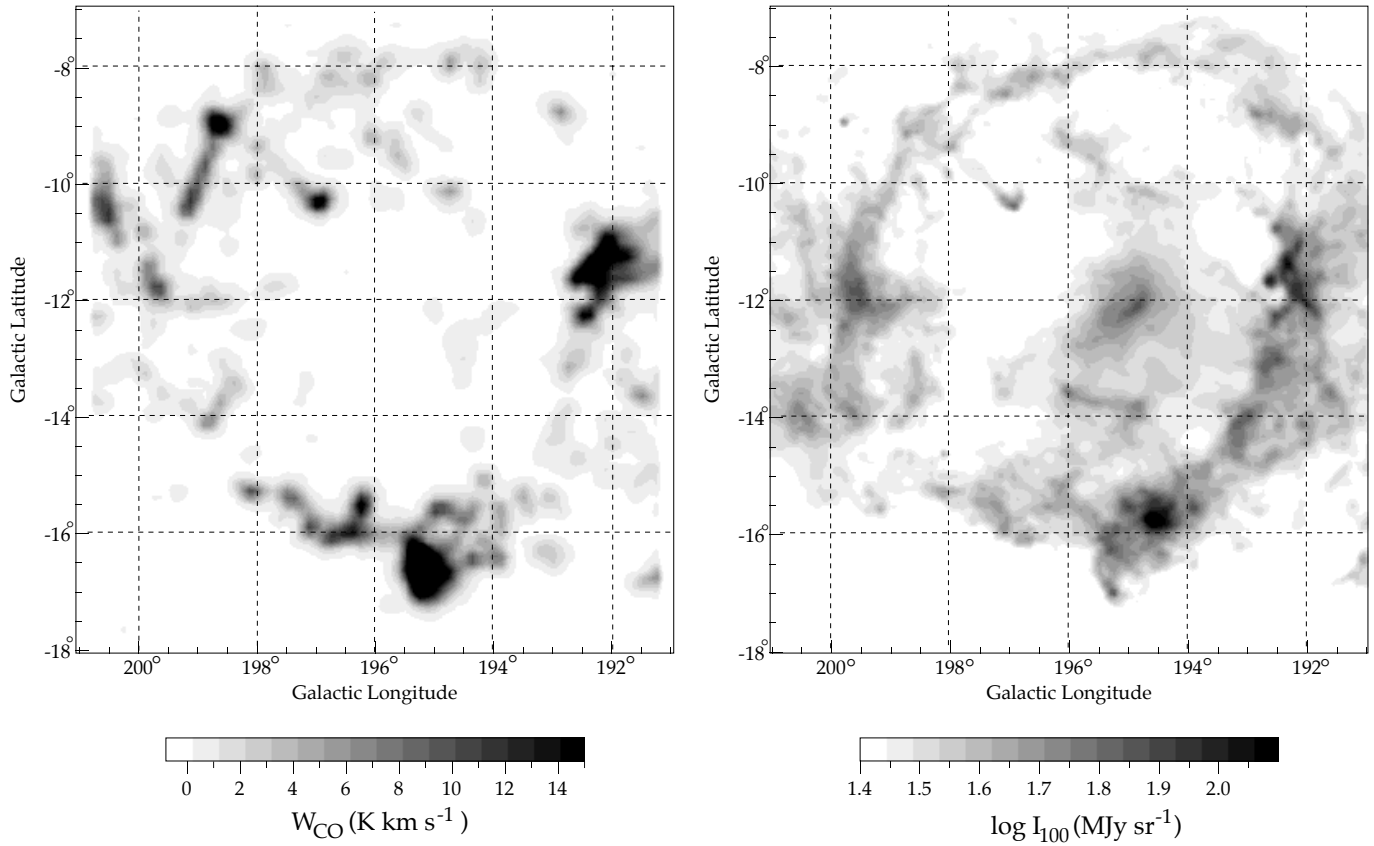


Fig. 10. The distribution of CO emission (left) compared with 100 μ m infra-red emission observed by IRAS (right).

does not follow the velocity gradient of the other clumps, and therefore may be either unrelated to the filament, or significantly perturbed.

The Southwestern Ring complex, and parts of the Ring's eastern edge, also display a less well defined velocity structure than the major clouds in the Ring. These regions are composed entirely of small, low-mass clumps. They contribute much of the continuous low-level FIR emission that gives the Ring its well-defined shape at 100 μ m. Clump velocities in the Southwestern Ring lie mainly in the 0 to 5 km s^{-1} range, reflecting their position midway between the B30 and B223 clouds. All of the emission is weak. There are no lines with peak temperatures greater than 3 K, hence very little of the structure of this part of the Ring was revealed in the MM survey.

4.4. The L1598/1599 complex

The strongest emission in the far northeastern section of the ring is from the dumbbell-shaped cloud containing the Lynds dark clouds L1598 and L1599. Optical images of the region are dominated by the foreground object α -Ori, and little other detail is visible in the POSS images. However, the positions of the optical obscuration correspond to the positions of the maxima of IRAS and CO emission at each end of the complex. The northern peak in emission (L1598) is clump 5 in the new CO survey, with a radial velocity of 11.4 km s^{-1} . The southern

peak (L1599) is clump 8, at 10.1 km s^{-1} . Together they have a mass of $\sim 600 M_{\odot}$.

4.5. B223

This complex differs from those in the rest of the Ring, in having a centroid velocity of around 0 km s^{-1} . It contains peaks MM 4 and 5 from the old survey and the small H II region Sh-2-263, which corresponds to a roughly circular hole in the CO emission around (195°, -16°). The ionizing source for the H II region is the B0 star, HD 34989.

The diffuse H II region Sh-2-265 lies on the southern side of the cloud. The steep CO contours surrounding clumps 3,4,6 and 7 follow the optical bright rims closely. These bright rims apparently face *away* from λ -Ori. This section of the cloud lies outside the Sh-2-264 H II region excited by the λ -Ori cluster, so the source of photodissociation and ionization must be something else. Possibilities include the other subgroups of the Orion OB1 association; Ori OB1b in particular, is density bounded to the north and west, allowing the UV-photons to reach the B223 cloud.

5. Comparison with 100 μ m emission

Qualitatively, the CO emission is well correlated with 100 μ m dust emission as seen by IRAS, as may be seen in Fig. 10. The molecular ring closely resembles the dust ring, and many of the

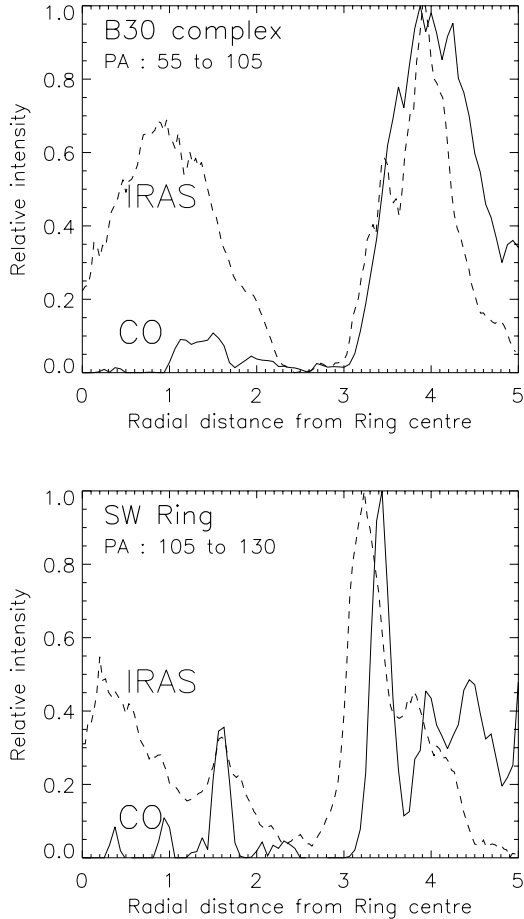


Fig. 11. Radial emission profiles for IRAS 100 μ m and W_{CO} emission. Each is plotted in units of relative intensity with the brightest emission as $I=1$. The position angles, PA, are measured West of Galactic North from a centre at $(196^\circ.1, -12^\circ.7)$

filamentary far-infrared structures have molecular counterparts. The main differences occur near the centre of the maps. Bright IRAS 100 μ m emission comes from the Ring interior, peaking in a plateau surrounding the central OB stars. Little CO emission is seen in this region. For example, the bright IRAS feature named the ‘bar’ by Zhang et al. (1989) is not detected in CO. The radio continuum emission at 1420 MHz from the H II region S-2-264 (Reich & Reich, 1986) is contained within the molecular region as expected. According to McKee et al. (1984), we should not find substantial molecular gas in the central region, as most clouds within the estimated homogenization radius of ~ 20 pc of λ -Ori will have been dissociated into atomic and ionized gas. However, a minimum in the radio emission around $l=194^\circ.5$, $b=-12^\circ$ and the presence of CO at a similar position and at the systemic velocity of the Ring (see Sect. 7) suggests that there are still the remains of the massive cloud which formed λ -Orionis itself. The radio minimum might be interpreted as a shadow cast by the remaining dense material creating a region less excited by the stellar UV than its surroundings.

The Ring possesses a remarkable degree of symmetry, at least in projection, so it is useful here to make the simplification

that it is a flat object lying in the plane of the sky, so that angular distance from the exciting star is proportional to radial distance. Radial profiles may then be made by averaging the emission in the CO and infrared maps in concentric circles around the Ring centre (as calculated in Sect. 7). The profiles for various objects were made by selecting ranges of position angles around the Ring and two of these, for B30 and the SW Ring, are shown in Fig. 11.

The prominent features in the IRAS profiles in both cases are the broad central region enclosing the OB stars, and the Ring emission between $r=3^\circ$ and 5° . The former is the result of excess dust heating by the strong UV-field, and the latter results mainly from the enhanced density in the Ring.

The FIR emission from the SW Ring (lower panel) peaks at $r \approx 3^\circ.2$. In contrast, the CO emission maximum is at $r \approx 3^\circ.4$. Indeed the broad features of the IRAS profile reproduce those of the CO, but offset by $0^\circ.2$ – $0^\circ.3$ inside them. In contrast, the main part of B30 (upper panel) has the CO and FIR emission peaking at about the same distance. However, the feature on the inside of the complex has its FIR emission peaking some $0^\circ.2$ further in than the CO. This is in the region of the optically bright rims reported by Zhang et al. (1989). Overall we find that this effect is not visible in the CO–bright clouds in B30, B35 and B223 and is most noticeable in the lighter, less structured clouds of which the SW Ring is the clearest example. Other examples are the Spur, the inner clouds in the N Ring and the outer clouds of the Arm. These features are consistent with the idea that much of the IRAS emission comes from the bright rims of clouds, where the UV-field substantially exceeds that of the interstellar background. This dust with temperature above 20 K is found in the photodissociation regions in the bright rims, where the CO emission drops off due to dissociation. From our maps it appears that these effects combine to form a region on the inside edges of the clouds, of thickness 1–2 pc, where CO abundance is reduced due to dissociation, and where the dust is over-luminous relative to standard ISM values.

6. The distribution of young stars

The stellar population in the vicinity of λ Orionis is apparently related to the distribution of gas and dust. The star formation history may be investigated by both optical and infrared observations. T Tauri stars are thought to be traced both by their $H\alpha$ emission and by their FIR emission as revealed by the IRAS Point Source Catalog (IPSC). Both these aspects of young stellar objects (YSOs) are therefore briefly examined in this section. $H\alpha$ is seen in ‘naked’ T Tauri stars, while the far infrared results can show emission from young stars still embedded within their parental clouds. The IRAS point sources would thus represent a younger epoch of star formation than the $H\alpha$ -stars. Unfortunately, in practice, these embedded IRAS sources are heavily confused by FIR cirrus from the surrounding dust and it was found impossible to make unambiguous identifications of enough YSOs by their IRAS properties to warrant a detailed study.

6.1. $H\alpha$ emission stars

Fig. 12 shows the positions of the $H\alpha$ emission-line stars from Duerr et al. (1982) relative to the CO emission and the central OB association. They are found predominantly in the northern section of the Ring, forming a belt of stars of dimensions $\sim 8^\circ \times 2^\circ$ stretching between the clouds B30 and B35, and passing across the region occupied by the OB-stars. Duerr et al. suggest that these $H\alpha$ stars are the ‘fossil’ remnants of the molecular cloud. Their correlation with the CO emission in the present survey suggests that B30 and B35 are the remains of this elongated primordial configuration

6.2. IRAS point sources

There are 1052 entries in the IRAS Point Source Catalog in the survey region. These were searched for sources detected in the $12\ \mu\text{m}$ and $25\ \mu\text{m}$ bands which have a flux density of $3.0\ \text{Jy}$ or greater at $60\ \mu\text{m}$, to avoid contamination from galaxies and Galactic cirrus clouds. Sources which have identifications in extragalactic and stellar catalogues were removed, yielding a sample of 12 objects. Most of these are probably YSOs, although it is difficult to make certain identifications on the basis of the IPSC alone as IRAS lacked adequate angular resolution to give clear contrast between the point sources and the background cirrus. Indeed, because of this many workers use additional information from, for example, optical extinction data. This useful approach is beyond the scope of the present work. The positions of the 12 objects are shown by * symbols on Fig. 12. Most of them lie in the same band outlined by the $H\alpha$ emission-line stars, reinforcing the idea that this is the region of star formation from which the λ -Ori association was born. If the stars in this band were formed contemporaneously then there is evidently a wide range of stellar mass from the massive OB stars down to low mass YSOs some of which are revealed by IRAS. There are insufficient objects in the Point Source sample to provide evidence of star formation in the Ring, triggered by the expansion of the H II region into the surrounding molecular material.

7. Modelling of kinematics

Because of the absence of much CO emission interior to the Ring, a spherical molecular shell with limb brightening accounts poorly for our data. Furthermore, inspection of Figs. 3 and 4 shows that almost all the emission at $b > -12^\circ 5$ has velocities greater than $5\ \text{km s}^{-1}$ whilst the velocities of that $b < -12^\circ 5$ are less than $5\ \text{km s}^{-1}$. This suggests that an expanding ring is an appropriate model to fit to the data.

The data have therefore been fitted to a model in which the expansion velocity is constant from a selected centre. In such a model the line of sight velocity varies sinusoidally with position angle from the centre. A least-squares fit to this sinusoid yields the line of sight component of the expansion velocity, the position angle of the line of nodes and the overall systemic velocity. The weight given to each point in the data cube was proportional to the strength of the CO emission.

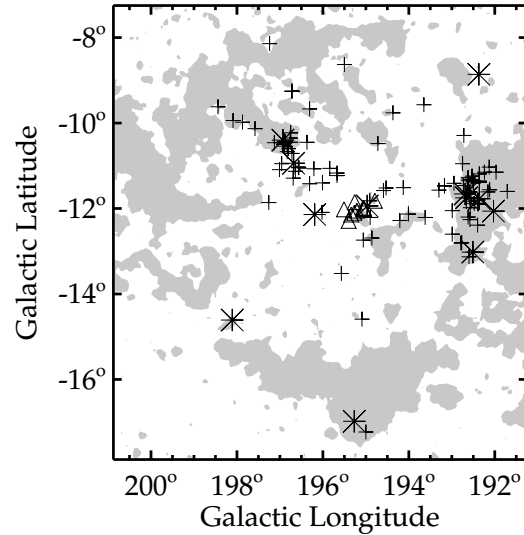


Fig. 12. $H\alpha$ emission-line stars (crosses) from the survey of Duerr et al. (1982), IRAS Point Sources (*) and OB-stars (Δ), compared with the CO. The regions within the lowest contour of Fig. 2 are shown in grey. λ -Ori is one of the OB-stars near $(195^\circ, -12^\circ)$. The figure emphasises the association of these stellar populations with the the B30 and B35 clouds.

A grid of positions of the expansion centre was searched for the minimum rms deviation and a well-defined but shallow minimum was found at $(195^\circ 5, -14^\circ 8)$, for a systemic velocity of $4.74\ \text{km s}^{-1}$ and a line-of-sight component of expansion velocity of $6.8\ \text{km s}^{-1}$. The rms deviation was $2.07\ \text{km s}^{-1}$, which may be compared with the average linewidth estimated at $2.2\ \text{km s}^{-1}$ (FWHM) from the velocity widths of the clumps shown in Table 2. On the assumption of approximately gaussian profiles, this FWHM corresponds to a standard deviation of $0.975\ \text{km s}^{-1}$. As the deviation of the model is only about twice this, it is considered to be a satisfactory fit.

A separate fit was made to the position of the emission on the sky, regardless of velocity. A simple fit for a circle yields a radius of $4^\circ 0$ with its centre at $(196^\circ 1, -12^\circ 7)$, with an rms deviation of $0^\circ 68$. The average FWHM of the clumps in Table 2 is $0^\circ 42$, corresponding for a gaussian shape to a standard deviation of $0^\circ 18$, so most of the deviation from the circle comes from the scatter of cloud positions. This ring fit is shown on Fig. 2. A further fit to an ellipse with its axis along the line of nodes of the velocity fit does not give a statistically improved fit having an rms deviation of $0^\circ 67$.

The most secure and useful results are those for the size of the Ring, $R_0 = 4^\circ 0$, the systemic velocity $V_0 = 4.74\ \text{km s}^{-1}$, and the line of sight component of the expansion velocity $V_{exp} \sin(i) = 6.8\ \text{km s}^{-1}$. The main difficulty in the interpretation of these results is the absence of information about the inclination, i of the Ring as this is needed to find the actual expansion velocity. An attempt was made to detect ellipticity in the projected image of the Ring to set an upper limit to the inclination, but this method is sensitive to minor distortions in the Ring shape due, for example, to differing ram pressures in different directions. A range of ellipses were fitted with various centres

and position angles. None gave rms deviations better than a simple circle fit, so are not statistically significant. No models with a deviation similar to the circle suggested that $\cos(i)$ should be less than 0.85, so there is no evidence that $\sin(i)$ is greater than 0.5, and a lower limit on the expansion velocity may be set at about twice our fitted value, ie 14 km s^{-1} .

The previous CO survey (MM) appeared to give a good ring-fit to the emission maxima, with a definite inclination with respect to the plane of the sky. But the Ring, as revealed by the newly-discovered emission in this survey, appears roughly circular ‘by eye’. This result is borne out by the objective analysis presented above, which shows that the Ring is statistically indistinguishable from a circular ring ‘face on’ to us in the plane of the sky. Suggestions of ellipticity and projected expansion velocity give us only very uncertain constraints as to the expansion rate and hence the age of the object. The distinct minimum in the velocity fit, at $V_{exp}\sin(i)=6.8 \text{ km s}^{-1}$, suggests that there is indeed an inclination to the ring, but the ring fit can give only an upper limit of about 30° , corresponding to the $V_{exp}=14 \text{ km s}^{-1}$ given above. Simple considerations of energy transfer from the OB stars to the Ring give only a very high (and therefore unlikely) upper limit of $V_{exp}=80 \text{ km s}^{-1}$. Thus the Ring’s low inclination makes it extremely unfavourable for precise measurements of expansion rate.

In a model in which the Ring encircles the H II region S-2-264, use can be made of the $H\alpha$ velocity measurements of Fich et al. (1990). They give a systemic velocity of 5.6 km s^{-1} , close to our value of 4.74 km s^{-1} . Their velocity width is 37.4 km s^{-1} , suggesting an expansion velocity of 18.7 km s^{-1} , consistent with our result. If this is also the expansion rate of the Ring, its inclination is 21° . However, this simple model should be treated with caution as the H II region expansion would be slowed by the denser molecular material.

It should be noted, however, that the lower bound here corresponds to a maximum Ring age of approximately 4 Myrs, assuming constant acceleration, which is consistent with previous estimates of the age of the OB-association (Murdin & Penston, 1977). For this reason, an inclination of around 30° is deemed most likely. This value implies a total energy in the expansion of $3 \times 10^{42} \text{ J}$, about 2×10^{-4} of the luminous output of the OB stars during the 4 Myrs.

8. Discussion

The IRAS data and the new CO data show that the H II region is surrounded by a remarkably complete ring, which nevertheless displays a highly fragmented substructure. Fragmentation by various instabilities may sometimes occur in the expansion of an H II region. However, it is not clear whether this “... induced clumpiness can be distinguished from primordial clumpiness.” (Dyson 1994).

Models of evolved expanding H II regions (Mazurek 1980) and of λ -Orionis specifically (MM) consider expansion into a uniform spherically symmetric or sheetlike molecular cloud. This naturally produces shell and ring structures, which may

gradually fragment into clumps which will tend to have low mass.

The clumps in the λ -Ori Ring seem to divide into two classes. The molecular features are either (i) diffuse, low mass clouds with relatively high clump-clump velocity dispersion, or (ii) dense, massive, dark globules. The Southwestern and Northern section of the Ring fall into the former category, while B30 and B223 are examples of the latter. In Sect. 4, we have demonstrated that there are possible differences between the two classes.

It is probable that the dense, higher mass clouds arise from the initial structure of within the GMC from which the Ring was formed. Fragmentation of a uniform shell/sheet is unable to account for the size and mass of these clumps over the lifetime of the Ring. Much of the complex substructure in the Ring today is therefore likely to have been determined by equally complex and uncertain initial conditions of the system, while the basic ring shape is the result of the expansion. The lower mass clumps may result from subsequent fragmentation. Initial inhomogeneity is also the most satisfactory explanation for the molecular material observed *inside* the Ring, where we would otherwise expect any CO to be fully dissociated.

Examples of similar dense filaments and globules exist within the Rosette Nebula (eg. White et al. 1997) and in IC1396 (Patel et al. 1995). It seems that such features are characteristic of nebulae around many O-stars (Gyul’budagyan et al. 1994). In many cases, the expanding shells/rings are fully ionized, and we only see emission from the dense clumps. In other such objects, it may just be that a survey was not sufficiently sensitive to detect the weaker CO emission from the diffuse, low-mass clouds, as was the case with λ -Ori prior to this survey.

Using these ideas in conjunction with the results of our survey enables us to postulate several possible histories of the Ring. Again it must be stressed, however, that incomplete knowledge as to primordial conditions within the entire Orion star-forming region makes these schemes inevitably speculative.

We have seen that the distribution of $H\alpha$ stars, OB-stars and IRAS point sources may well delineate the edge of a primordial GMC complex which dominated the northern half of the survey area, ~ 4 Myrs ago. There may have been in addition a southern GMC, with each of the clouds having a mass of $\sim 6000 M_\odot$. Each cloud would have been elongated in shape, running at approximately constant Galactic Latitude and with little depth in the plane of the sky. If the clouds were to collide at a speed typical of the standard cloud-cloud velocity dispersion, 4 km s^{-1} , then the shocked gas at the interface will remain molecular. The compression may lead to Jeans instability and star formation within the interface zone. Massive star formation would then produce UV-fields and winds to ionize and sweep up the surrounding ISM into a ring. Certain parts of the Ring (eg. the Northern and Southwestern sections) would contain mainly swept up gas, while the denser sections remain to trace the original locations of the clouds.

There are variations on this theme consistent with the data, particularly as there now appears to be a degree of interaction between the southern clouds (notably B223) and the rest of

the Ori OB1 association, along with the Ori-Eri Bubble and Barnard's Loop. Thus we can also envisage a scheme in which star formation in a highly inhomogeneous primordial GMC is induced via an external trigger, such as supernovae in the Ori OB1a subgroup, or stellar winds from the 1b or 1c subgroups to the southeast.

In conclusion, we only have weak constraints on the expansion of the λ -Ori Ring due to its orientation. Even so, it is apparent that the evolution of the Ring does not fully correspond to simple models of expanding rings or shells into a homogeneous medium. The original conditions within the parental cloud(s) are a major influence on the Ring's present-day appearance, which in turn are inextricably linked with the structure and history of the Orion star forming region as a whole, the details of which are still far from clear.

9. Conclusions

Reviewing the new CO data, in conjunction with previous surveys, enable us to draw the following conclusions:

1. The evolved H II region Sh-2-264 is expanding from the λ -Orionis OB-association, which is <4 Myr old.
2. Surrounding the H II region is a toroidal ring of molecular gas and dust. Some of this material has been swept up by the expansion, but most is the remains of the parent GMC, which had two major components. The ring has been expanding for up to 4 Myr.
3. The OB-stars and the H α emission-line stars may have formed at roughly the same time, in an extended band along the southern edge of the northern cloud.

Acknowledgements. WJL and MRWM would like to thank the Center for Astrophysics for hospitality extended and D Hartmann, C. Lada and J Dyson for useful discussions and comments. We thank the journal referee, J. Wouterloot for his helpful comments.

References

- Barnard E.E., 1894, *Knowledge* 17, 17
 Barnard E.E., 1927, in: *Atlas of Selected Regions of the Milky Way*, eds. E.B. Frost, M.R. Calvert, Carnegie
 Bence S.J., Richer J.S., Padman R., 1996, *MNRAS* 279, 866
 Benson P.J., Myers P.C., Wright E.L., 1984, *ApJ* 279, L27
 Bertoldi F., McKee C.F., 1992, *ApJ* 395, 140
 Blitz L., 1991, In: C.J. Lada, N.D. Kylafis (eds) *The Physics of Star Formation and Early Stellar Evolution*. Kluwer, p. 125
 Cabrit S., Goldsmith P.F., Snell R.L., 1988, *ApJ* 334, 196
 Cohen R.S., Dame T.M., Thaddeus P., 1986, *ApJS* 60, 695
 Cunha K., Smith V.V., 1996, *A&A* 309, 892
 Dame T.M., Elmegreen B.G., Cohen R.S., Thaddeus P., 1986, *ApJ* 305, 892
 Digel S.W., Hunter S.D., Mukherjee R., 1995, *ApJ* 441, 270
 Digel S.W., Lyder D.A., Philbrick A.J., Puche D., Thaddeus P., 1996, *ApJ* 458, 561
 Duerr R., Imhoff C.L., Lada C.J., 1982, *ApJ* 261, 135
 Dyson J.E., 1994, In: *Star Formation and Techniques in Infrared and mm-Wave Astronomy*, Springer-Verlag p 114.
 Fich M., Treffers R.R., Dahl G.P., 1990, *AJ* 99, 622
 Gyl'budagyan A.L., Oganyan G.B., Akhverdyan L.G., 1994, *Astrophysics* 37, 317
 Hartmann D., Burton W.B., 1997, *An Atlas of Galactic Neutral Hydrogen*. CUP
 Khavtassi D.S., 1960, *Atlas of Galactic Dark Nebulae*. Bull. Abastumanskaya Astrofiz Obs. 18, 29
 Kutner M.L., Tucker K.D., Chin G., Thaddeus P., 1977, *ApJ* 215, 521
 Leisawitz D., Bash F.N., Thaddeus P., 1989, *ApJS* 70, 731
 Lynds B.T., 1962, *ApJS* 7, 1
 Mazurek T.J., 1980, *A&A* 90, 65
 Maddalena R.J., Morris M., 1987, *ApJ* 323, 179 (MM)
 Maddalena R.J., Moscowitz J., Thaddeus P., Morris M., 1986, *ApJ* 303, 375
 Maloney P., 1990, *ApJ* 348, L9
 McKee C.F., Van Buren D., Lazareff B., 1984, *ApJ* 278, L115
 Morgan W.W., Strömgren B., Johnson H.M., 1955, *ApJ* 121, 611
 Murdin P., Penston M.V., 1977, *MNRAS* 181, 657
 Myers P.C., Heyer M., Snell R.L., Goldsmith P.F., 1988, *ApJ* 324, 907
 Oliver R.J., Masheder M.R.W., Thaddeus P., 1996, *A&A* 315, 578
 Pan S.-K., Feldman M.J., Kerr A.J., Tinbie P., 1983, *App. Phys. Lett.* 43, 786
 Patel N.A., Goldsmith P.F., Snell R.L., Hezel T., Xie T., 1995, *ApJ* 447, 721
 Reich P., Reich W., 1986, *A&AS* 63, 205
 Reich W., 1978, *A&A* 64, 407
 Sharpless S., 1959, *ApJS* 4, 257
 Sugitani K., Fukui Y., Mizuni A., Ohashi N., 1989, *ApJ* 342, L87
 Sugitani K., Fukui Y., Ogura K., 1991, *ApJS* 77, 59
 Wade C.M., 1957, *AJ* 62, 148
 Wade C.M., 1958a, Ph.D. Thesis, Harvard University
 Wade C.M., 1958b, *Review of Modern Physics* 30, 946
 White G.J., Lefloch B., Fridlund C.V.M., et al., 1997, *A&A* 323, 931
 Williams J.P., de Geus E.J., Blitz L., 1994, *ApJ* 428, 693
 Wilson R.E., 1963, *General Catalogue of Stellar Radial Velocities*. Carnegie
 Zhang C.Y., Green D.A., 1991, *AJ* 101, 1006
 Zhang C.Y., Laureijs R.J., Chlewicki G., Wesselius P.R., Clark F.O., 1989, *A&A* 218, 231
 Zhou S., Butner H.M., Evans N.J., 1988, *ApJ* 333, 809